Investigation of Microbubble-enhanced Mild Hyperthermia with Focused Ultrasound for Drug Delivery Enhancement

Kaleb Vuong

A dissertation

submitted in partial fulfillment of the

requirements for the degree of

Master of Science in Bioengineering

University of Washington

2023

Reading Committee:

Mike Averkiou, Chair

Adam Maxwell, Member

Program Authorized to Offer Degree:

Bioengineering

University of Washington

Abstract

Investigation of Microbubble-enhanced Mild Hyperthermia with Focused Ultrasound for Drug Delivery Enhancement

Kaleb Shilong Vuong

Chair of the Supervisory Committee:
Mike Averkiou
Department of Bioengineering

Conventional methods for treating cancer include the use of systemic chemotherapeutic drugs. However, due to the tumor's low drug uptake, high doses of these drugs are needed for effective treatment, which can result in adverse side effects. Research has shown that elevating the temperature of the tumor by 5-10 ℃, defined as mild hyperthermia, results in increased drug uptake of the tumor. Heating of the tumor can be performed via High Intensity Focused Ultrasound (HIFU) however, HIFU focuses energy onto a millimeter size area. Prior work has shown that adding microbubbles during HIFU can enhance the heating. It was suggested that there exists an optimal microbubble concentration that varies with respect to acoustic pressure amplitude that results in enhanced heating and larger lesion formation for ablative purposes. However, no group has investigated bubble-enhanced heating in the context of inducing mild

hyperthermia over a larger area. In this work, we first identified and characterized three media that allowed for uniform dilution of microbubbles, developed a robust technique of thermocouple alignment, measured temperature elevation with and without microbubbles of varying concentrations and varying acoustic pressure amplitudes in the characterized media, and imaged microbubble behavior including destruction during heating treatment. Our results showed that solid gel phantoms were more similar to human tissue in terms of acoustic properties and allowed for more reliable temperature measurements. Despite acoustic streaming of the fluid media, our temperature measurements showed that as the acoustic pressure amplitude increases, the optimal microbubble concentration needed for inducing enhanced temperature elevation at the focus decreases. This is due to acoustic streaming where at higher concentrations, attenuation also increases such that the heating occurs prefocally, resulting in little or no enhancement in temperature rise. We were able to induce focal temperature elevation relevant for mild hyperthermia in the gelatin evaporated milk phantom when heating at a focal pressure of 1.5 MPa and 10^4-10^5 MBs/mL. Via imaging, we confirmed that the microbubble destruction path changes as microbubble concentration and pulse length changes, which affects where and how much heating occurs in the media. Real time imaging of the microbubbles allowed us to identify that after the first six heating pulses (1.074 MHz, focal pressures of 1.5-2 MPa, 400K cycles), most of the microbubbles that contribute to bubble-enhanced heating at the focus have been destroyed. Furthermore, as the pulse length increases so does the extent of microbubble destruction. Our findings underscore the importance of having a real-time image guidance during ultrasound treatment and the need to further investigate the effects of microbubble concentration and acoustic pressure amplitude for further optimizing heating relevant for mild hyperthermia.

TABLE OF CONTENTS

LIST OF FIGURES

LIST OF TABLES

Chapter 1. INTRODUCTION

Cancer is classified as a complex heterogenous disease in which abnormal cells develop and divide without control and invade other tissues within the body [1]. This occurs when the necessary processes that regulate cell division are no longer functioning and are often a result of mutated DNA and abnormal gene expression. Cancer ranks as one of the leading causes of death and acts as a barrier to increasing life expectancy in every country of the world [2]. In 2020, it was estimated that 18.1 million new cancer cases and 9.9 million cancer deaths occurred globally. By 2040, it is expected that there will be 28 million new cancer cases and 16.2 million cancer deaths. Within the US, an estimated 1.9 million new cases of cancer along with 609,000 cancer related deaths are projected to occur in 2023 [3]. Although there have been numerous advancements in cancer treatment, chemotherapy is the most used method of treating advanced cancers [4]. These drugs target and kill fast-growing cells within the body, which is effective in treating cancer as tumor cells are known to grow and multiply much quicker than most cells in the body. However, the main limitation of using chemotherapy for cancer treatment is the low uptake of such drugs [5]. In order to overcome this low uptake, a larger concentration gradient of chemotherapeutic drugs is needed for the tumor to absorb an effective dosage [6]. However, these drugs are also toxic to normal tissue, which limits the concentration gradient that can be administered. One of the reasons for low uptake is because the tumor has poor vascularity and defective lymphatic drainage, which results in high interstitial fluid pressure that prevents sufficient drug uptake [7]. Furthermore, the tumor's extracellular matrix (ECM) has been shown to be stiffer than the ECM of normal tissue, which serves as another barrier to efficient drug delivery via preventing effective diffusion of drug into tumor cells [8]–[10].

Through the use of microbubbles and ultrasound, the delivery of chemotherapeutic agents into the tumors has been enhanced both preclinically[11]–[17] and clinically[18], [19]. Microbubbles are small (1-10 micrometers) gas spheres that are stabilized by a lipid, protein, or polymeric shell that respond via expansion and contraction when interacting with an ultrasonic pulse [20]. Under certain acoustic conditions, microbubbles have been shown to transiently perforate and permeate cellular membranes, which is commonly referred to as sonoporation and has been shown to increase drug uptake within the tumor through mechanical effects. Another method of enhancing drug uptake within the tumor focuses on thermal effects and is through the use of mild hyperthermia, which is defined as a sustained temperature of 39-45 °C for 30-60 minutes [21], [22]. By inducing mild hyperthermia within the tumor, physiological changes such as increased tumor blood flow, enhanced vascular permeability, increased oxygenation, decreased interstitial fluid pressure, and reestablishment of normal physiological pH conditions occur [23]. In doing so, studies have shown the efficacy of chemotherapy and radiotherapy has improved in solid tumors when combining mild hyperthermia with the aforementioned therapies. Ultrasound can be used to induce localized temperature rise within the body. High intensity focused ultrasound (HIFU) is currently used as an ablative tool for treating essential tremors and cancers [24], [25]. In the context of inducing mild hyperthermia, HIFU may not be favorable as the treated volume can be small in comparison to a tumor's volume. This requires the HIFU source to be continually displaced to treat the entire tumor volume, which results in long treatment times [26]. Microbubbles have been shown to enhance ultrasound's heating capabilities by reducing the amount of energy needed for equivalent temperature rise when heating without microbubbles. Recent work has explored the effects of microbubble concentration and acoustic pressure amplitude in the context of ablative temperatures in an egg white phantom [27]. They found that

there exists an acoustic pressure threshold needed for bubble-enhanced heating and that the concentration of microbubbles affected the ablative lesion's shape and position. Juang et al. investigated bubble-enhanced heating using HIFU and commercial microbubbles in both a non-perfused porcine liver and ex vivo machine-perfused porcine liver, which allowed for a study that better replicated conditions relevant to in vivo unlike the egg white phantoms [28]. They explored the effects of acoustic pressure as well as the method of delivery of contrast agents on focal temperature elevation. From their work, they observed enhanced temperature elevation and increased area of heating when using HIFU with microbubbles. Thus, with the use of microbubbles, it may be possible to reduce treatment times as a larger volume of heating is performed, reducing the need for continual displacement of the HIFU source. Similar to Clark et al., this work primarily focused on temperature elevation relevant for ablation and not mild hyperthermia.

No group has studied the effects of microbubble concentration and acoustic pressure amplitude in the context of inducing mild hyperthermia. My work seeks to investigate the effects of microbubble concentration and acoustic pressure amplitude in the context of inducing localized mild hyperthermia in both a fluid and solid gel phantom. There are two major aims to the present work: 1) Investigate and characterize various tissue mimicking media that can house dilute microbubbles, 2) Investigate temperature elevation with and without the presence of microbubbles in those media. The first aim will be accomplished by identifying fluid and solid media that are microbubble friendly, then measuring their acoustic properties. Lastly, the second aim will be achieved by developing a robust method of thermocouple alignment, then taking thermocouple temperature elevation measurements in those media without microbubbles and with microbubbles at varying concentrations and at varying acoustic pressure amplitudes. In

addition, microbubble destruction will be imaged which will serve as a visual connection between microbubble destruction and bubble-enhanced heating.

A brief overview of all the chapters in this work are as follows: in chapter 2, materials and methods involved in all experiments conducted are shown; in chapters 3 and 4, the results of each experiment are shown alongside a discussion of our findings, and lastly in chapter 5, findings will be summarized and concluded.

Chapter 2. MATERIALS AND METHODS

2.1 MODELING OF ULTRASOUND-INDUCED TEMPERATURE ELEVATION

Computational modeling of the heat generated from ultrasound propagation into a known medium is based on the Pennes' Bioheat equation shown below [29].

$$\rho c_p \frac{\partial T}{\partial t} = K\nabla^2 T + Q + Q_p + Q_m$$

The Pennes' Bioheat equation is often used in studying heat transfer in biological systems as it considers the effect of external energy sources i.e., ultrasound as well as heat transfer within the medium via metabolic processes and perfusion. It describes the temperature change based on certain parameters that are biologically relevant. Q is the volumetric heat deposition due to ultrasound, Q_p is heat loss due to blood perfusion, and Q_m is the heat term due to metabolic processes. ρ is density of medium, C_p is the specific heat, T is temperature, t is time, κ is heat conductivity, and $\nabla^2 T$ is the 3D spatial second derivative of heat ($\nabla^2 = \partial_x^2 + \partial_y^2 + \partial_z^2$). Due to the Bioheat equation being a 3D partial differential equation, computational methods rely on the use of finite difference methods to compute an approximate solution. The theoretical heat generation will be used to identify optimal ultrasound parameters that are necessary for identifying mild hyperthermia conditions without microbubbles and used as a starting point.

For the use of simulating *in-vitro* experiments, the Bioheat equation can be simplified by ignoring heat from biological processes. Thus, heat due to metabolism and perfusion are neglected. The simplified equation is shown below.

$$\rho c_p \frac{\partial T}{\partial t} = K\nabla^2 T + Q$$

Q is derived from various properties of the propagation medium as well as the ultrasound intensity, and defined as the following:

$$Q = 2\alpha I$$

I is the ultrasound intensity and α is the absorption coefficient of the medium. I is proportional to p^2 (where p is pressure at any spatial location in the defined field) and is defined as:

$$I(x,y,z) = \frac{p_0^2(\frac{p}{p_0}(x,y,z))^2}{2\rho c} e^{-2\alpha z}$$

p_0 is the source pressure and is dependent on the amount of energy input into the ultrasound transducer. c is the speed of sound through the medium. The normalized pressure field $\frac{p}{p_0}(x,y,z)$ can be found using the Rayleigh integral. The Rayleigh integral is a linear acoustic pressure field model that assumes continuous wave propagation.

The partial differential equation can be numerically solved via finite difference methods. In particular, our model will use the forward time centered space method. By doing this, the spatial second derivative $\nabla^2 T$ is shown as follow:

$$\nabla^2 T = \frac{T(x-\Delta x,y,z,t) - 2T(x,y,z,t) + T(x+\Delta x,y,z,t)}{\Delta x^2} + \frac{T(x,y-\Delta y,z,t) - 2T(x,y,z,t) + T(x,y+\Delta y,z,t)}{\Delta y^2} + \frac{T(x,y,z-\Delta z,t) - 2T(x,y,z,t) + T(x,y,z,+\Delta z,t)}{\Delta z^2}$$

The first derivative of temperature with respect to time can be simplified as well and is shown below:

$$\frac{\partial T}{\partial t} = \frac{T(x,y,z,t+\Delta t) - T(x,y,z,t)}{\Delta t}$$

By substituting in the defined equations above into the Bioheat equation and isolating for $T(x, y, z, t + \Delta t)$, the results is shown as follow:

$$
\begin{aligned}
&T(x, y, z, t + \Delta t) \\
&\quad = \frac{\kappa \Delta t}{\rho C_p}\left(\frac{T(x - \Delta x, y, z, t) - 2T(x, y, z, t) + T(x + \Delta x, y, z, t)}{\Delta x^2}\right. \\
&\quad + \frac{T(x, y - \Delta y, z, t) - 2T(x, y, z, t) + T(x, y + \Delta y, z, t)}{\Delta y^2} \\
&\quad \left. + \frac{T(x, y, z - \Delta z, t) - 2T(x, y, z, t) + T(x, y, z, +\Delta z, t)}{\Delta z^2}\right) + \frac{\Delta t}{\rho C_p} Q(x, y, z) \\
&\quad + T(x, y, z, t)
\end{aligned}
$$

From this equation, one can iteratively solve the temperature at a single point by using the previous surrounding temperature points in space known from the boundary conditions. We will use this model to estimate the temperature rise in homogeneous media.

2.2 Fabrication and Evaluation of Tissue Mimicking Media for Administration of Diffuse Microbubbles

Throughout this work, three media were used in evaluating temperature elevation with and without the presence of diffuse microbubbles, which consisted of

(1) 66% (v/v) glycerol-water solution,

(2) 5% (w/v) porcine gelatin phantom, and

(3) 5% (w/v) gelatin evaporated milk (GEM) phantom.

For a 150 mL sample, 100 mL of glycerol (Sigma-Aldrich Corp., St Louis, MO, USA) and 50 mL of degassed deionized (DI) water is added to a beaker. With the beaker on a stir plate, the mixture is stirred until mixture appears homogenized. Once that has occurred, the mixture is

allowed to rest for at least half an hour before pouring into a Flex-Hinge plastic box (FT-42, TAP Plastics, Seattle, WA). The 5% (w/v) porcine gelatin phantom consists of the following materials: degassed DI water and 300 gel strength type A porcine skin gelatin (Sigma-Aldrich Corp. St. Louis, MO, USA). A known volume of DI degassed water is added to a beaker on a stir plate. Then 5% w/v (weight is in grams and volume is in milliliters) of gelatin is gradually added to the beaker whilst vigorously stirring. Once all of the gelatin is added and incorporated into the water, the mixture is allowed to heat to 75 Celsius (mixture should become clear at this point) whilst stirring gradually (stirring speed was set to half to two-thirds of the initial speed). The solution is then allowed to cool down until the solution reaches 32 Celsius in which case the solution is poured into Flex-Hinge plastic box(es) and are placed into the refrigerator for at least an hour, which allows for the solution to fully solidify within the plastic box. Lastly, the 5% (w/v) GEM phantom consists of the same materials as the porcine gelatin phantom with the addition of evaporated milk (Nestlé Carnation Evaporated Milk: Vitamin D Added). Method for fabrication was modified from a phantom recipe [30] and follows the same procedure described previously for the 5% porcine gelatin phantom, except a 1:1 volume ratio of degassed DI water and evaporated milk is used instead of pure degassed DI water. In the case where microbubbles are present in the gelatin-based phantoms, dilute microbubble solutions were prepared, then added and mixed into the gelatin solution before putting the plastic boxes into the refrigerator. Medium (2) and (3) are used up within 2 hours after removal from the fridge.

During bubble-enhanced heating measurements, dilute microbubble solutions were prepared, then added and mixed into the various media studied. For the 66% glycerol-water solution phantom, an in-house “Definity-like” microbubble [31], [32] were used. For these dilutions, we assumed an initial vial concentration of 1×10^9 MBs/mL. A triple dilution was then performed

to create 3 different concentrations: 10^4-10^6 MBs/mL within the 66% glycerol-water solutions. For gelatin-based phantoms, Sonazoid (GE Healthcare Inc., Amersham, UK) microbubbles were used. These microbubbles were prepared according to the manufacturer's instructions and a starting vial concentration of 1×10^9 MBs/mL was assumed [33]. Three different concentrations were also evaluated, and the microbubble dilution is performed as follows. Microbubbles were first diluted by a factor of 10^3 then 0.1, 1, or 10 mL of that diluted solution were added and mixed thoroughly into the gelatin solution, which we will deem low (10^4 MBs/mL), medium (10^5 MBs/mL), and high concentration (10^6 MBs/mL), respectively.

All relevant acoustic properties of the three media were measured. Such properties included density, speed of sound, and attenuation. For the gelatin-based phantoms, density measurements were performed by measuring the mass of a piece of phantom then placing that piece into a volumetric beaker with a known volume of water in it and measuring the displacement that occurs. Density was then calculated by dividing the mass value by the volumetric displacement. For the 66% glycerol-water solution, density was calculated by multiplying the percent composition of each fluid by their respective densities and summing those values. Speed of sound and attenuation were measured by coupling two ultrasound transducers to the plastic box that contains the tissue mimicking medium. An experimental setup for this measurement is shown in Figure 2.1. The speed of sound through the medium was quantified by comparing the time of flight through the box when it contained deionized water to the time of flight through the box when it contained a tissue-mimicking phantom. This was done using the formula below:

$$c_{phantom} = \frac{l}{ToF_{phantom} - ToF_{water} + \frac{l}{c_{water}}}$$

where $c_{phantom}$ is the speed of sound through the tissue-mimicking phantom (m/s), c_{water} is the speed of sound in water (measured at 1492 m/s), $ToF_{phantom}$ is the time of flight of sound through the box containing the tissue-mimicking phantom, ToF_{water} is the time of flight of sound through the box containing water, and l is the interior width of the plastic box.

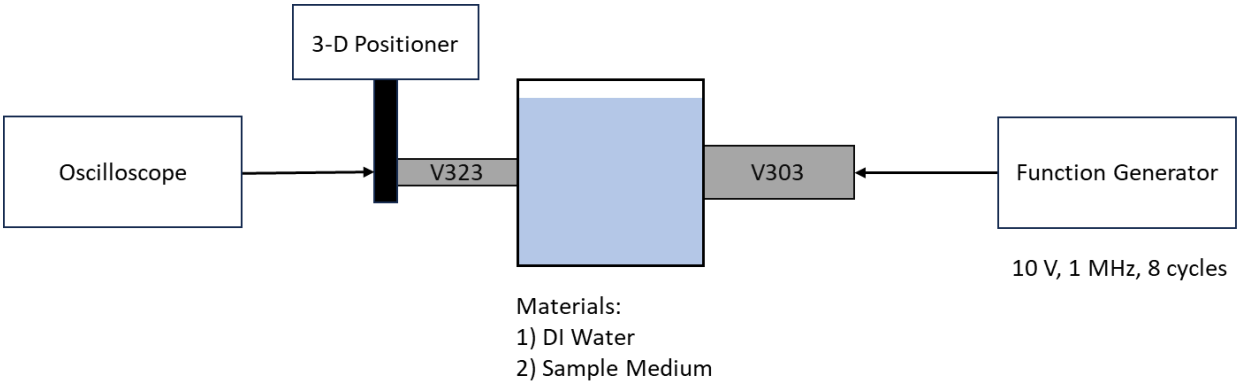

Figure 2.1. Experimental setup used for measuring speed of sound and attenuation of any medium used in this work. Each measurement in the sample medium was compared to the measurements performed in deionized water. V303 (diameter = 1.27 cm, frequency = 1.00 MHz; Olympus NDT, Waltham, MA, USA) was used as the transmitter and V323 (diameter = 0.64 cm, frequency = 2.25 MHz; Olympus NDT, Waltham, MA, USA) was used as the receiver.

To measure the attenuation coefficient of the medium, the peak-to-peak magnitude of the received signal was recorded when the box was filled with a.) deionized water, and b.) tissue-mimicking phantom. Assuming the walls of the box were thin so impedance could be ignored, the attenuation coefficient can be estimated as the ratio of received signal magnitudes over the interior length of the box relative to the attenuation in deionized water (assumed to be 0.025 Np/m):

$$\alpha = 0.025 - \frac{ln\left(\frac{V_{phantom}}{V_{water}}\right)}{l}$$

where α is the attenuation coefficient of the tissue-mimicking phantom, l is the interior width of the box, and $V_{phantom}$ and V_{water} are the peak-to-peak magnitudes of the received waveform when the plastic box contains a phantom or deionized water, respectively.

2.3 Ultrasound Induced Temperature Measurements

The experimental setup for heating experiments, illustrated in Figure 2.2, consisted of a tissue-mimicking phantom housed in a plastic box that was partially submerged in the degassed water tank. A needle thermocouple was used to monitor temperature and was inserted into a 19G needle (not shown) to prevent the thermocouple tip bending during insertion into phantoms. The phantom was insonified from the side by a focused transducer (focal distance = 4.45 cm, diameter = 4.45 cm, frequency = 1.074 MHz) submerged in the water tank and aligned to the tip of the thermocouple, which is positioned to be roughly in the center of the plastic box in axis 1. Tissue phantoms were insonified continuously for 30 s at 1.074 MHz and focal pressures of 0.5-3 MPa at 100% duty cycle or 81.94% duty cycle (440,000 cycle pulse every 500 ms). In bubble-enhanced heating experiments, an imaging probe (L12-3; Philips EPIQ, Philips Healthcare) was used to monitor the microbubbles within the phantoms in real-time during treatment. For each heating experiment, temperature was recorded every 0.1 s (10 Hz sampling rate) for 70 total seconds, where the first 10 seconds are to measure ambient temperature, followed by 30 s of ultrasound being on, and then 30 s of ultrasound off and the phantom is cooling.

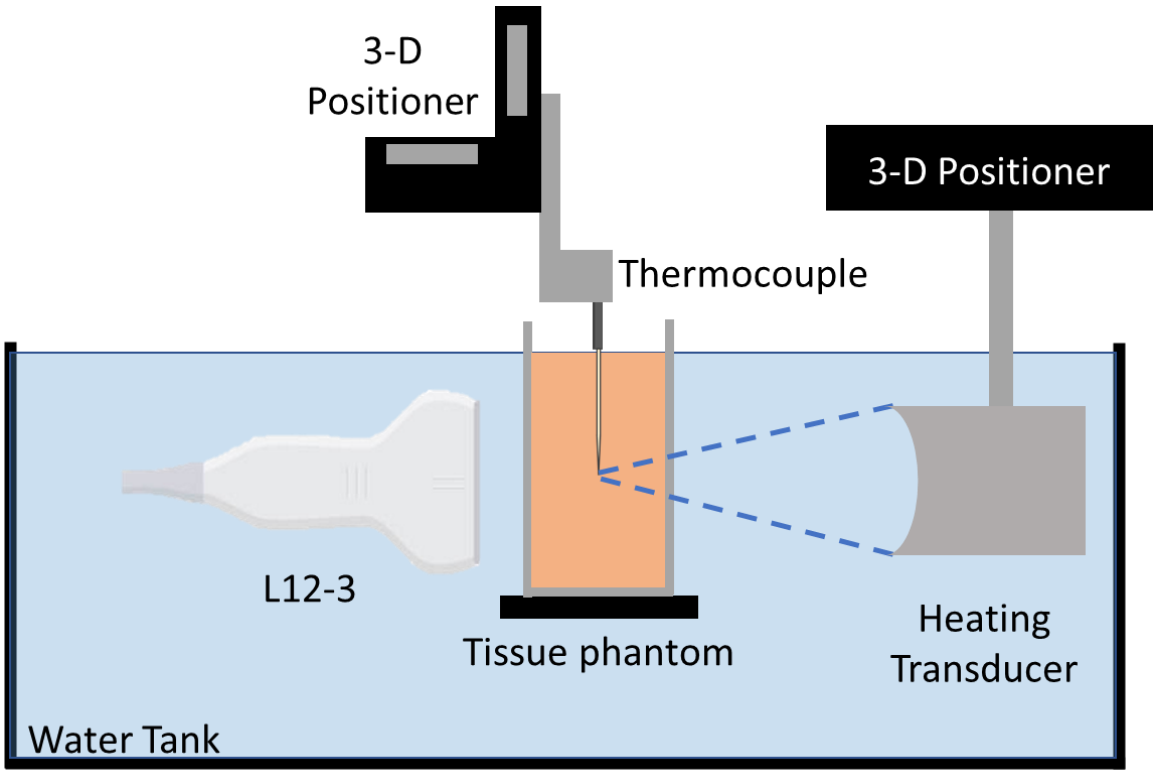

Figure 2.2. Schematic of setup used during heating experiments. The thermocouple is placed to be at the geometric center of the tissue mimicking phantom mold, with the maximum pressure produced from the heating transducer aligned with the thermocouple tip. L12-3 was coaligned with the focused transducer and used to monitor microbubbles in the phantoms during treatment in real time.

The alignment of the thermocouple, imaging probe, and heating transducer occurs in 3 stages when no sample box is present: 1.) Visual alignment of imaging probe with heating transducer and thermocouple in the absence of the phantom, 2.) pulse-echo/physical alignment of the heating transducer and thermocouple, and 3.) translate thermocouple to stage 1 alignment. Stages 1 and 3 are only necessary when an imaging probe was used as part of the experiments, and following this procedure allows for placement of the thermocouple tip within $\pm 0.5\ mm$ of the maximum pressure region of the heating transducer without the need for low-amplitude heating. Once alignment was complete, the thermocouple was lifted ~ 40 mm along axis 3 such that the

sample box with the phantom can be placed as shown in Fig. 2.2 and then lowered back into the sample medium. Below are more details on alignment of each of the 3 stages.

In stage 1, an imaging probe (L12-3) was used to roughly align the thermocouple and the beam path of the heating transducer. Visualization of the thermocouple was possible due to incomplete linear signal cancellation in the nonlinear amplitude modulation mode of the imaging probe [34]. By adjusting the position of the thermocouple, we can maximize the reflection of the thermocouple, where maximum intensity corresponds to the thermocouple being orthogonal to the imaging plane. For visualization of the heating transducer beam path, we utilized the radiofrequency (RF) interference signal (Figure 2.3) produced when the amplifier connected to the heating transducer is active and the function generator is turned on and transmitting at low input voltage (20 mVptp). This RF signal creates an artifact on imaging visible in both fundamental and contrast imaging settings. By adjusting the Axis 2 position of the heating transducer, the intensity of this artifact can be maximized which represents the heating transducer aligned with the imaging plane. Finally, the convergence point of this RF artifact is aligned with the tip of the thermocouple reflection as seen in Figure 2.3. It is important to note that the appearance of the RF artifact is not an exact match to the beam path of the heating transducer, but this visual representation allows us to roughly position all components of the setup before finer alignment in later steps. The current position of each setup component is saved as their home position, so changes in later alignment steps are relative movements and can be corrected in stage 3.

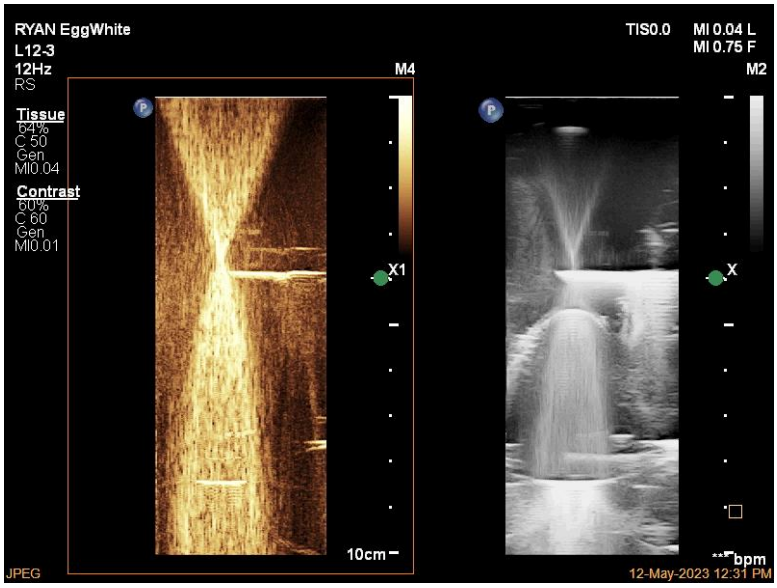

Figure 2.3. Contrast (left, bronze) and fundamental (right, gray scale) image of the RF artifact (bright hourglass shape) generated by HIFU source (amplifier on, function generator on at 20 mVptp). The thermocouple (horizontal bright line) can also be seen. The tip of the TC can then be visually aligned with the convergence point of the RF artifact (not shown).

In stage 2, we utilize a pulse-echo technique and the geometry of the heating transducer to place the tip of the thermocouple at the maximum pressure region. The pulse-echo technique consists of the heating transducer acting as a transmitter and receiver in a pulse-echo mode, while the thermocouple acts as a reflective surface. By connecting the oscilloscope and function generator to the heating transducer we can resolve the transmitted and reflected signals. By adjusting the position of the heating transducer on Axis 2 (Figure 2.2), we can maximize the received signal, where the maximum amplitude corresponds to the transverse alignment of the thermocouple and transducer. In Axis 1, the heating transducer's focal distance is converted to a time delay, which accounts for the time for the sound to travel to the thermocouple and reflected back to the transducer. This time delay is used to determine when the start of the reflected signal should occur, which corresponds to the axial alignment of the transducer and thermocouple as well as the maximum pressure region of the transducer. For Axis 3, the geometry of the heating

transducer is used for alignment. The diameter of the housing of the heating transducer was measured with calipers to find the radius of the housing. During this step, the heating transducer is positioned to be below the thermocouple. The heating transducer is then carefully moved until the thermocouple tip is approximately 0.2 mm above the housing. Then, the heating transducer is then shifted back to its original position in axis 1, and the heating transducer is moved upwards by a distance equal to the radius of the housing. When compared to low-amplitude heating, we found this geometric shift technique to have a systematic error of $+1\,mm$ where the thermocouple is originally placed too high and the heating transducer is translated upwards.

In stage 3, the final positions from stage 2 of the heating transducer and thermocouple are recorded and compared to the home positions established at the end of stage 1. The relative movements on all 3 axes are then calculated and used to move the transducer and thermocouple from stage 2 positions to the corresponding stage 1 positions. This ensures that the transducer and thermocouple are still aligned but have been placed within the imaging plane of the observation probe.

After alignment of all setup components, the thermocouple is raised to place the plastic box containing the tissue phantom and stage directly below the thermocouple as seen in Figure 2.2. The thermocouple is then manually lowered back to its aligned position. Manual removal and reinsertion (via micro positioners) of the thermocouple was tested with low-amplitude heating for potential misalignment over multiple iterations and no shifting of the maximum temperature position was observed. This setup then allows for various boxes containing different media to be switched in and out of the setup to quickly study heating in various tissue-mimicking phantoms.

2.4 Monitoring of Microbubble Destruction During Heating Via Ultrasound

During bubble-enhanced heating measurements, microbubble destruction was imaged in real time with the L12-3 linear array of a Philips EPIQ scanner. Side by side contrast-fundamental images were acquired. Imaging was interleaved with heating such that an image is acquired every 500 ms (2 Hz sampling rate), with imaging on for 62.5 ms (16 Hz PRF) and heating on for 409.7 ms (440,000 cycles, 1.074 MHz frequency; duty cycle of 81.94%). A mechanical index of 0.11 and gain of 60% allowed for sufficient imaging of the microbubbles whilst accounting for the attenuative nature of the GEM phantom.

To better visualize the microbubble destruction during the first 3 seconds of heating, we needed to minimize the RF artifacts displayed in our ultrasound images. Thus, another set of imaging experiments were performed without thermocouple temperature measurements with the same microbubble concentrations used in heating experiments. The same imaging probe and settings were used, however, instead of a 440,000 cycles heating pulse 400,000 cycles pulse was used instead. In addition, single pulses of 1,000, 10,000, and 100,000 pulses were also evaluated. A mechanical index of 0.10 and a gain of 57% was used as this improved the quality of the contrast images. Instead of firing 60 heating pulses with a pulse being fired every 500 ms, a single heating pulse, as well as 6 heating pulses with a single pulse firing every 500 ms were used. Images of the phantoms were acquired before and after the pulse(s) were fired to visualize the microbubble destruction path without the presence of the RF artifact and allowed for clear microbubble destruction over time whilst replicating the conditions used during heating experiments.

Chapter 3. RESULTS

3.1 Characterization of Tissue Mimicking Phantom's Acoustic Properties

As mentioned earlier, the goal of this work was to study the effects of microbubble concentration on heating via high intensity focused ultrasound. This means that the first criteria of the medium were the ability to suspend diluted microbubbles. Various fluid and solid phantoms were evaluated throughout this work; only 3 media were considered ideal candidates: (1) 66% (v/v) glycerol-water solution (fluid), (2) 5% (w/v) porcine gelatin phantom (solid), and (3) 5% (w/v) GEM phantom (solid). The addition of xanthan gum at various concentrations to 66% glycerol-water solution was attempted. We had hypothesized increasing the viscosity of the solution would aid in increasing attenuation. This resulted in a more viscous fluid medium that easily entrapped air bubbles during the mixing process and was difficult to degas entrapped air bubbles. Usage of pure glycerol did not fair well as glycerol had a density (1.26 g/cm^3) high enough that forced all microbubbles to quickly float to the top of the fluid even after stirring. The next criteria of the phantoms were acoustic similarity to human tissue [35], as the goal was to have an in-vitro phantom model that mimicked properties present in human tissue.

Table 3.1 summarizes the acoustic properties of the tissue mimicking phantoms used in this study. Also shown are literature values that are representative of the acoustic properties relevant to human tissue. The 66% glycerol-water solution had acoustic properties that differed greatly from human tissue. This medium was still investigated as it was easy to fabricate and allowed us to study the effects of bubble-enhanced heating in a fluid medium. The porcine gelatin and GEM phantom had densities and speed of sounds similar to human tissue. In addition to being able to

compare against human tissue properties, our measurements served as parameters for simulating temperature rise within the media that were studied.

Table 3.1. Measured acoustic property values for tissue mimicking phantoms used in this work and literature property values for human tissue.

Medium	Density (g/mL)	Speed of Sound (m/s)	Attenuation (dB/cm/MHz)
66% (v/v) glycerol-water solution	1.17	1810	0.1
5% (w/v) porcine gelatin phantom	1.05	1500	0.05
5% (w/v) GEM phantom	1.06	1520	0.32
Human Tissue	1.06	1540	0.5

3.2 Temperature Elevation Without Microbubbles

Temperature elevation measurements were taken without the presence of dilute microbubbles as this gave us insight into the heating behavior within the three media investigated. In doing so, we were able to identify certain settings that we would further investigate by introducing dilute microbubbles at varying concentrations. Figure 3.1 shows the temperature rise measured by the thermocouple in 66% glycerol-water solution at various focal pressures compared against modeled temperature elevation. At 1 MPa and 1.5 MPa, the 66% glycerol water solution temperature elevation curves deviated greatly from the modeled temperature elevation, which was due to streaming of the fluid, which would cause the fluid to mix. This can be seen as the highest temperature elevation recorded occurred before the 30 seconds of heating. The lowest focal pressure (0.5 MPa) tested did not exhibit noticeable streaming behavior, but we were only able to measure a maximum temperature elevation of 0.12 ºC. When compared to the modeled temperature elevation, there is noticeable discrepancy between the two heating curves. This was

attributed to possible streaming, misalignment errors, and/or errors associated with the acoustic and thermal properties used in modelling.

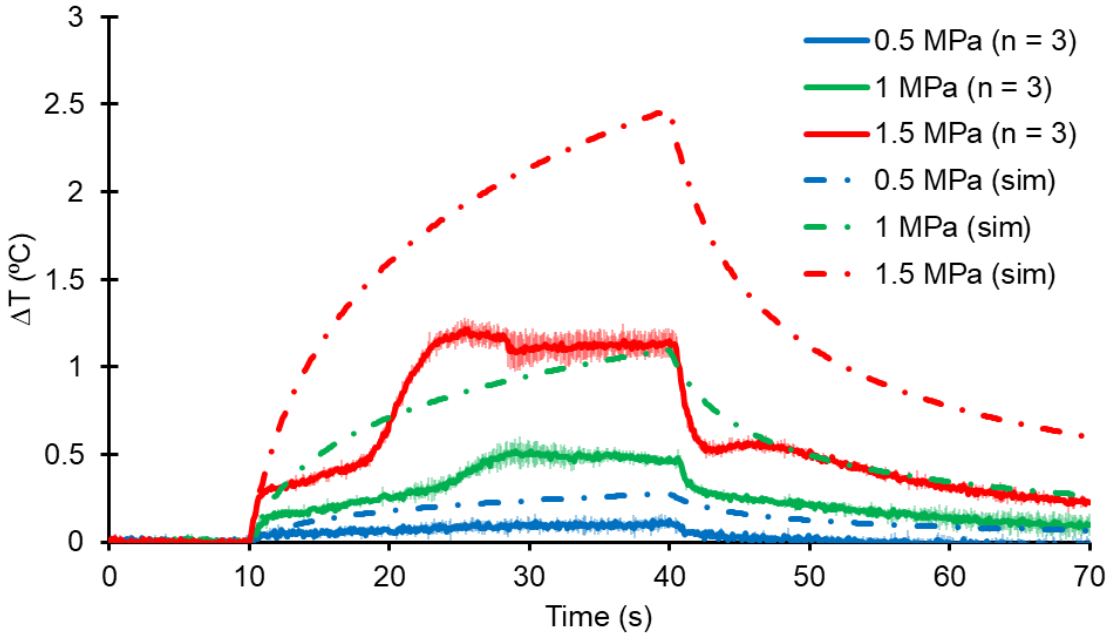

Figure 3.1. Heating measurements of 66% glycerol-water solution (n = 3) at various focal pressures (measured in water) at 100% duty cycle: 0.5 MPa, 1 MPa, and 1.5 MPa. Shaded standard deviation are included for all measurement. Measurements are compared alongside modeled temperature elevation as dashed colored lines.

Figure 3.2 shows the temperature rise measured by the thermocouple in the porcine gelatin phantoms (n = 3) at various focal pressures compared against modeled temperature elevations. At the tested focal pressures of 1, 2, and 3 MPa, the thermocouple measured a maximum temperature elevation of 0.58, 2.45, and 5.62 ºC, respectively. When compared to the modeled temperature elevation curves, the measured temperature elevation curves display similar behaviors but are of lower temperature rise at all acoustic pressure amplitudes. Since we did not measure the thermal properties of the porcine gelatin phantoms, it was estimated based on

published values [36]–[38]. Thus, the difference between measured and modelled temperature elevation may be due to differences in thermal properties used in modeling and actual properties.

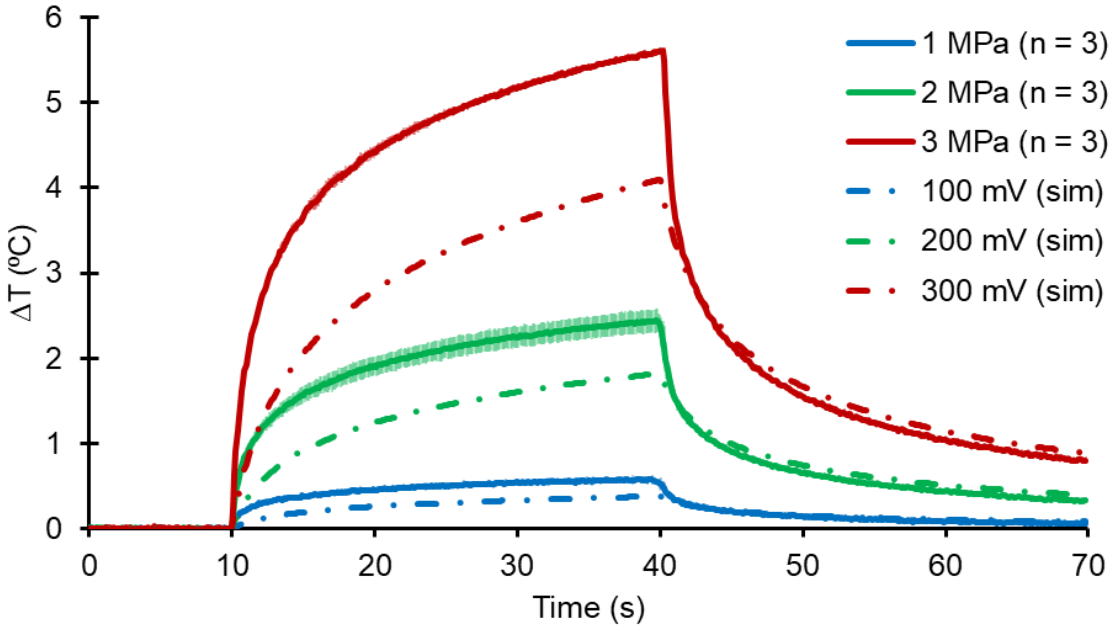

Figure 3.2. Heating measurements of 5% (w/v) porcine gelatin phantoms (n = 3) at various focal pressures (measured in water) at 100% duty cycle: 1 MPa, 2 MPa, and 3 MPa. Shaded standard deviation are included for all measurements. Measurements are compared alongside modeled temperature elevation.

Figure 3.3 shows the temperature rise measured by the thermocouple in the GEM phantoms (n = 3) at various focal pressures compared against modeled temperature elevations. At the tested focal pressures of 1, 1.5, and 2 MPa, the thermocouple measured a maximum temperature elevation of 1.57, 4.21, and 8.75 ºC, respectively. A smaller focal pressure range was studied in the GEM as we had wanted to account for an increased attenuation compared to the porcine gelatin phantoms. Like the porcine gelatin phantoms, the measured heating curves were similar to the modeled temperature elevation curves since no streaming is present. Differences between modeled temperature elevation and measured were also attributed to using incorrect thermal

properties in our model as we were not able to measure these properties (specific heat and thermal diffusivity).

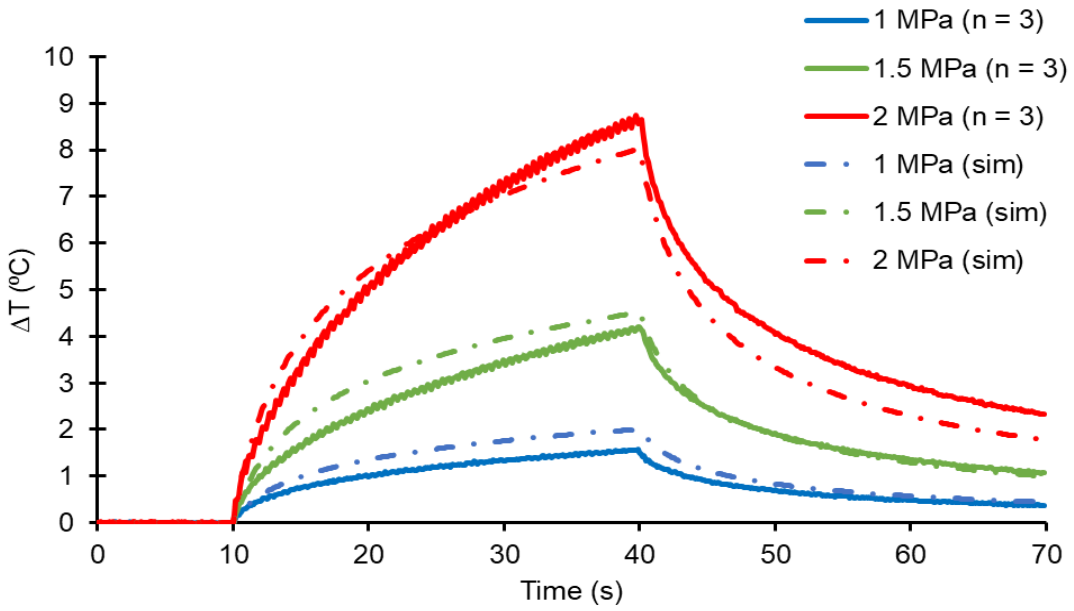

Figure 3.3. Heating measurements of 5% (w/v) GEM phantoms (n = 3) at various focal pressures (measured in water) at 81.94% duty cycle: 1 MPa, 1.5 MPa, and 2 MPa. Shaded standard deviation are included for all measurements. Measurements are compared alongside modeled temperature elevation.

3.3 Temperature Elevation With Microbubbles

Since the goal of this work was to investigate the effects of varying dilute microbubble concentration on elevated temperature elevation for mild hyperthermia purposes, it had been decided that conditions that resulted in temperature elevation below 5 ºC were deemed ideal for further investigation. For the 66% glycerol-water solution, focal pressures of 1 and 1.5 MPa were chosen. Although these pressures resulted in streaming within the fluid, they also generated noticeable temperature elevation that may be enhanced by the presence of dilute microbubbles. For the porcine gelatin, focal pressure of 2 MPa was evaluated as we had measured a maximum

temperature elevation of 2.45 ºC, whichis below mild hyperthermia. For the GEM phantoms, focal pressures of 1 MPa and 1.5 MPa were evaluated further as the maximum measured temperature elevations were below our defined mild hyperthermia range.

Figure 3.4 and Figure 3.5 show the temperature rise measured by the thermocouple in 66% glycerol-water solution at a focal pressure of 1 and 1.5 MPa, respectively, at varying dilute microbubble concentrations of 10^4-10^6 MBs/mL. At a focal pressure of 1 MPa, all microbubble concentrations resulted in an immediate temperature rise during the first second of heating, showing that bubble-enhanced heating has been measured. At the lowest microbubble concentration of 10^4 MBs/mL, the thermocouple measurements show no enhancement in heating when compared to the control case (No MBs). With a microbubble concentration of 10^5 MBs/mL, thermocouple measurements show that a maximum temperature elevation of 0.92 ºC occurs after 8.3 seconds of heating. Then after this point, the recorded temperature elevation decays and plateaus as heating continues. At the highest dilute microbubble concentration of 10^6 MBs/mL, the thermocouple measurements show a different behavior from the other microbubble concentrations tested. Temperature rise occurs throughout the whole duration of heating, resulting in a maximum temperature elevation of 2.59 ºC. From these measurements, it seems that the highest microbubble concentration resulted in enhanced heating at the focus.

When heating the 66% glycerol-water solution at a higher focal pressure of 1.5 MPa at the same dilute microbubble concentrations of 10^4-10^6 MBs/mL, different trends emerged (Fig. 3.5). In similarity with the lower focal pressure heating in Fig. 3.4, enhanced temperature rise occurred within the first second of heating, which suggests that bubble-enhanced heating has occurred. At a dilute microbubble concentration of 10^4 MBs/mL, a maximum temperature elevation of 1.96 ºC. The heating curve shows that most of the temperature rise occurs during the first second of

heating and the temperature rise measured plateaus onwards even as the medium is still being heated. At the middle concentration of 10^5 MBs/mL, the heating curves shows an immediate temperature rise to 1.4 ºC during the first second of heating then followed by decrease. After 10s of heating has occurred, the thermocouple measurements show an increase in temperature with a maximum temperature rise of 2.02 ºC. With a microbubble concentration of 10^6 MBs/mL, a temperature rise of 1 ºC occurs during the first second of heating then is followed by a gradual rise as heating continues to a maximum temperature elevation of 2.49 ºC. Based on the thermocouple measurements, the maximum measured focal temperature rise occurred when heating with the highest microbubble concentration.

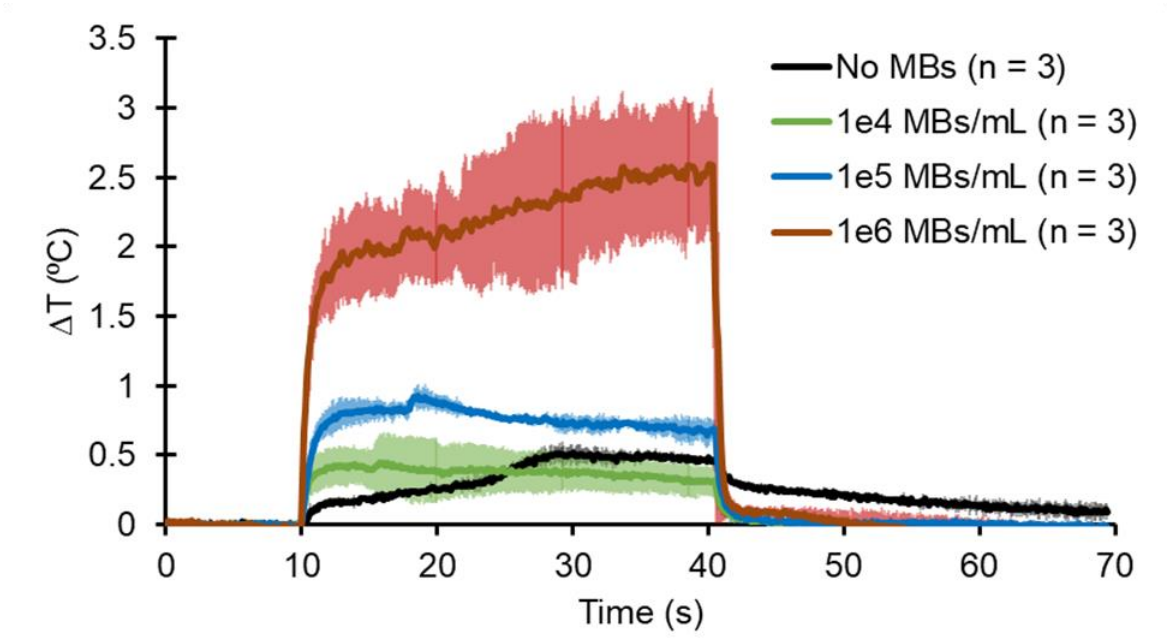

Figure 3.4. Heating measurements of 66% (v/v) glycerol-water solution (n = 3) with varying dilute microbubble concentration at 1 MPa focal pressure (measured in water) at 100% duty cycle. Shaded standard deviation are included for all measurements.

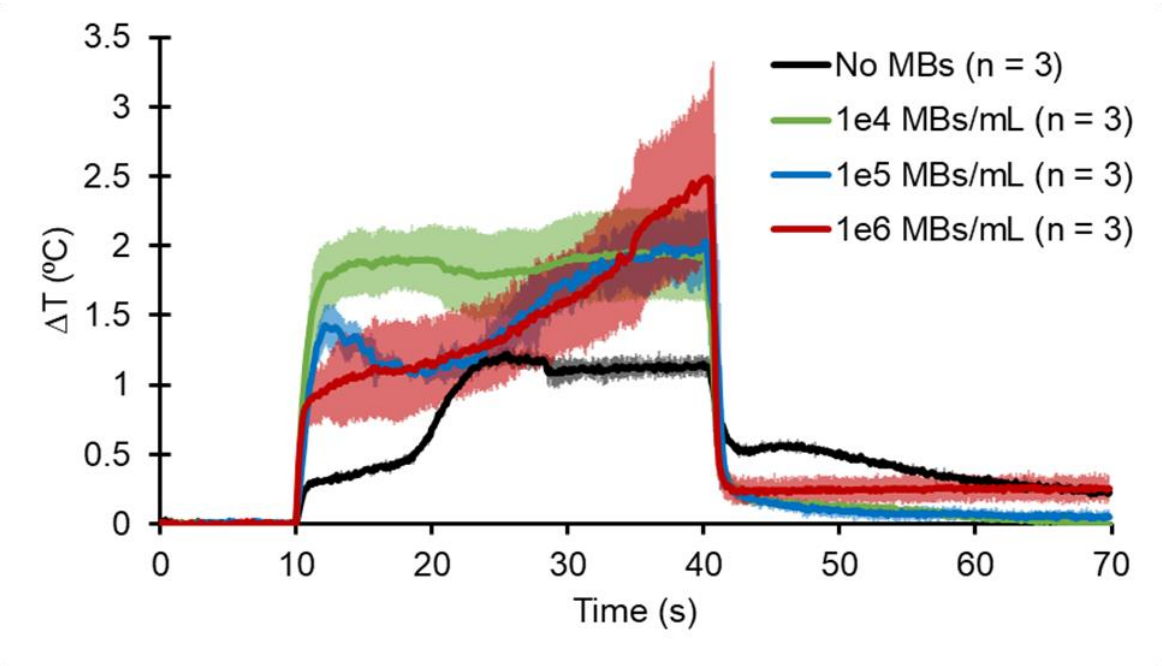

Figure 3.5. Heating measurements of 66% (v/v) glycerol-water solution (n = 3) with varying dilute microbubble concentration at 1.5 MPa focal pressure (measured in water) at 100% duty cycle. Shaded standard deviation are included for all measurements.

Thermocouple temperature rise measurements in porcine gelatin phantoms at a focal pressure of 2 MPa for varying dilute microbubble concentrations is shown in Figure 3.6. At all microbubble concentrations, elevated focal temperature rise was measured. Higher focal temperature rise occurred at the lower concentrations, with a maximum temperature elevation of 4.48 ºC. At the medium and high concentrations, a maximum temperature elevation of 3.90 ºC and 2.99 ºC were measured, respectively. An immediate temperature rise during the first second of heating was only measured with the low and medium concentrations whilst the high concentration did not show any signs of immediate temperature rise when compared to the control phantoms, which is suggestive of acoustic shadowing. The high concentration had enough microbubbles to attenuate the transducer's beam path prefocally, which results in the heating to occur closer to the transducer. Thus, the thermocouple which is aligned to transducer's focus was not able to

measure an immediate temperature rise as observed in the low and medium concentrations. In conclusion, the low microbubble concentration resulted in maximized temperature elevation when compared to the control phantoms. An additional 2.04 ºC was measured at the focus whilst the medium and high concentration had an addition of 1.46 ºC and 0.54 ºC, respectively. Only one thermocouple measurement was performed in the porcine gelatin phantom with addition of dilute microbubbles as this was an initial exploration into measuring bubble-enhanced heating in a solid phantom with entrapped dilute microbubbles with the goal of reaching mild hyperthermia conditions. Due to the low attenuation of the porcine gelatin phantoms, we had decided to investigate bubble-enhanced heating in a more attenuative solid phantom such as the GEM phantom.

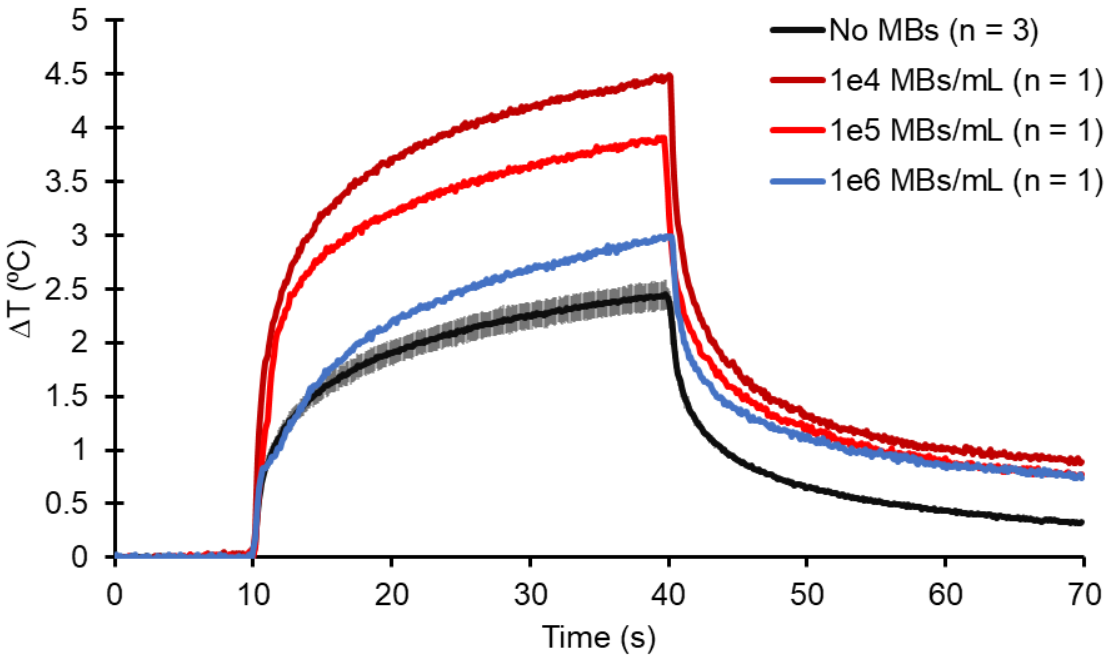

Figure 3.6. Heating measurements of 5% (w/v) porcine gelatin phantoms (n = 1) with varying dilute microbubble concentration at 2 MPa focal pressure (measured in water) at 100% duty cycle. Shaded standard deviation are included for all measurements with multiple trials.

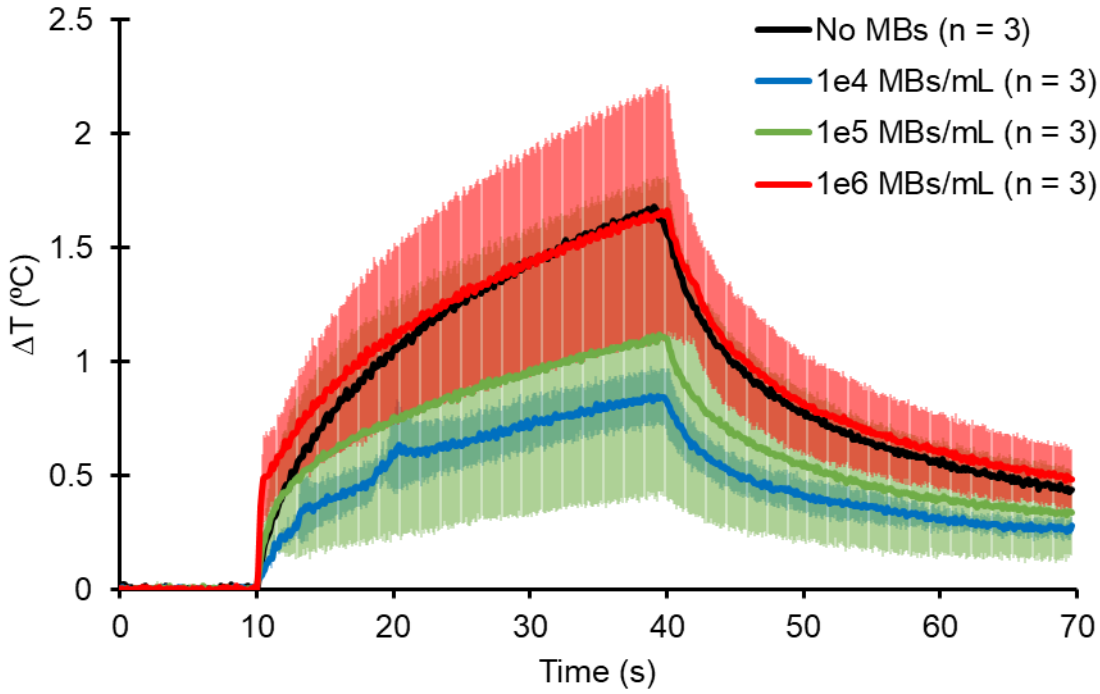

Figure 3.7. Heating measurements of 5% (w/v) GEM phantoms (n = 3) with varying dilute microbubble concentration at 1 MPa focal pressure (measured in water) at 81.94% duty cycle. Shaded standard deviation are included for all measurements with multiple trials.

Temperature measurements in GEM phantoms at a focal pressure of 1 MPa at varying dilute microbubble concentrations are shown in Figure 3.7. All phantoms were heated at a duty cycle of 81.94% to allow for interleaved imaging of the phantoms with a clinical probe. From our thermocouple measurements, we observed no significant enhancement in heating regardless of microbubble concentration. From low to high microbubble concentration, a maximum temperature elevation 0.84 ºC, 1.11 ºC, and 1.66 ºC was measured. In the control phantoms, we measured a maximum temperature rise of 1.67 ºC. Furthermore, these measurements have a much greater variance than the measurements at the higher focal pressures, which could be due to human error during fabrication of the GEM phantoms with dilute microbubbles. To summarize, at a focal pressure of 1 MPa we were not able to measure bubble-enhanced heating

at the concentrations tested. At this pressure, we may have not reached the pressure threshold needed for cavitation activity, which would contribute to elevated temperature rise enhancement. Based on the trends observed in these curves, at this focal pressure a higher microbubble concentration may yield enhanced heating at the focus.

Figure 3.8 shows temperature rise measurements in GEM phantoms at a focal pressure of 1.5 MPa with the same microbubble concentrations in Figure 3.7. At all dilute microbubble concentration, the maximum measured temperature elevation is higher than the control phantom. In addition, compared to the control phantom, a higher temperature rise occurs within the first second of heating. The medium concentration resulted in the highest maximum temperature rise of 6.11 ºC whilst the low and high concentrations resulted in a maximum temperature rise of 5.65 ºC and 4.91 ºC, respectively. Thus, a low and medium microbubble concentration resulted in mild hyperthermia conditions at the focus when heating with source pressures that did not result in mild hyperthermia conditions without microbubbles. When comparing to the control phantom, the medium microbubble concentration resulted in an additional increase of 1.9 ºC at the focus, which was highest enhancement in heating at the focus out of all microbubble concentrations investigated.

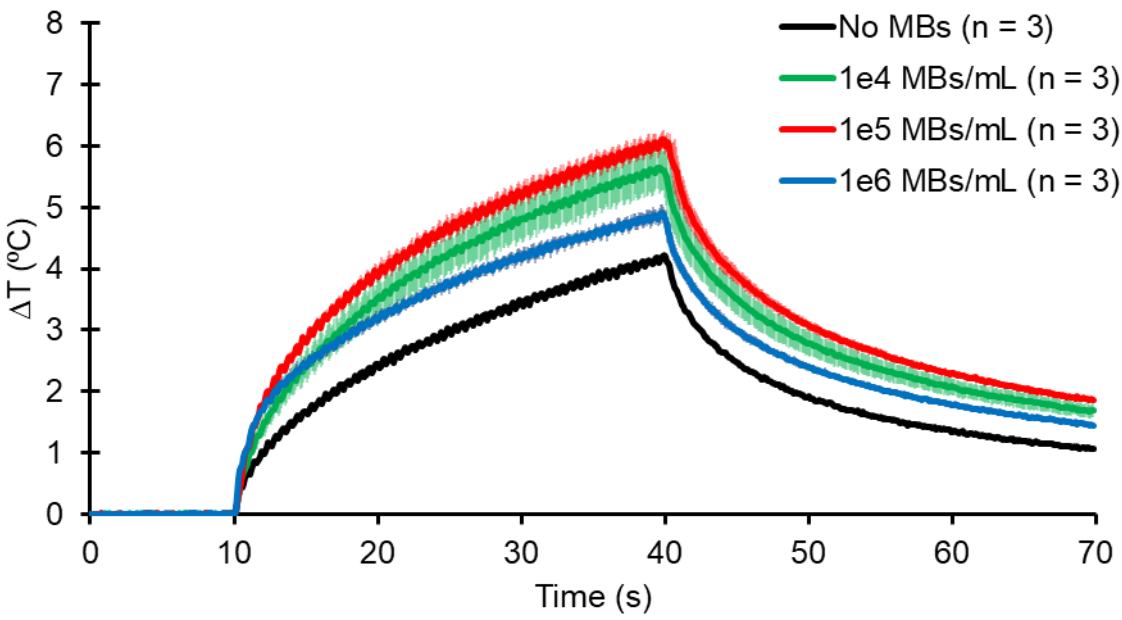

Figure 3.8. Heating measurements of 5% (w/v) GEM phantoms (n = 3) with varying dilute microbubble concentration at 1.5 MPa focal pressure (measured in water) at 81.94% duty cycle. Shaded standard deviation are included for all measurements with multiple trials.

3.4 Microbubble Destruction During Ultrasound Induced Heating

Figure 3.9 shows ultrasound images taken for three different microbubble concentrations (low C: 10^4 MBs/mL, med C: 10^5 MBs/mL, high C: 10^6 MBs/mL) at 1.5 MPa focal pressure that are taken at different time points during the heating experiment: t = 0 s, which occurs before our heating transducer is on, t = 0.5 s, which occurs after the first pulse of 440,000 cycles is fired, t = 15.5 s, which represents the halfway point of our heating duration, and t = 30.5, which occurs after the heating transducer is turned off. Ultrasound from the heating transducer propagates from bottom to top in the images. The bright horizontal reflector in the middle right of the contrast image is from the thermocouple. At t = 0.5s, microbubbles within the HIFU beam path are destroyed. At all microbubble concentrations, the initial HIFU pulse is not able destroy all of the microbubbles in the beam path as shown by comparing t = 0.5 s to t = 15.5 s ultrasound

images. During the middle of heating, we observed that destroyed microbubble outline decreases in width as microbubble concentrations increases. Furthermore, at higher microbubble concentrations, the converge of the beam path shifts closer to the transducer, appearing lower than the thermocouple.

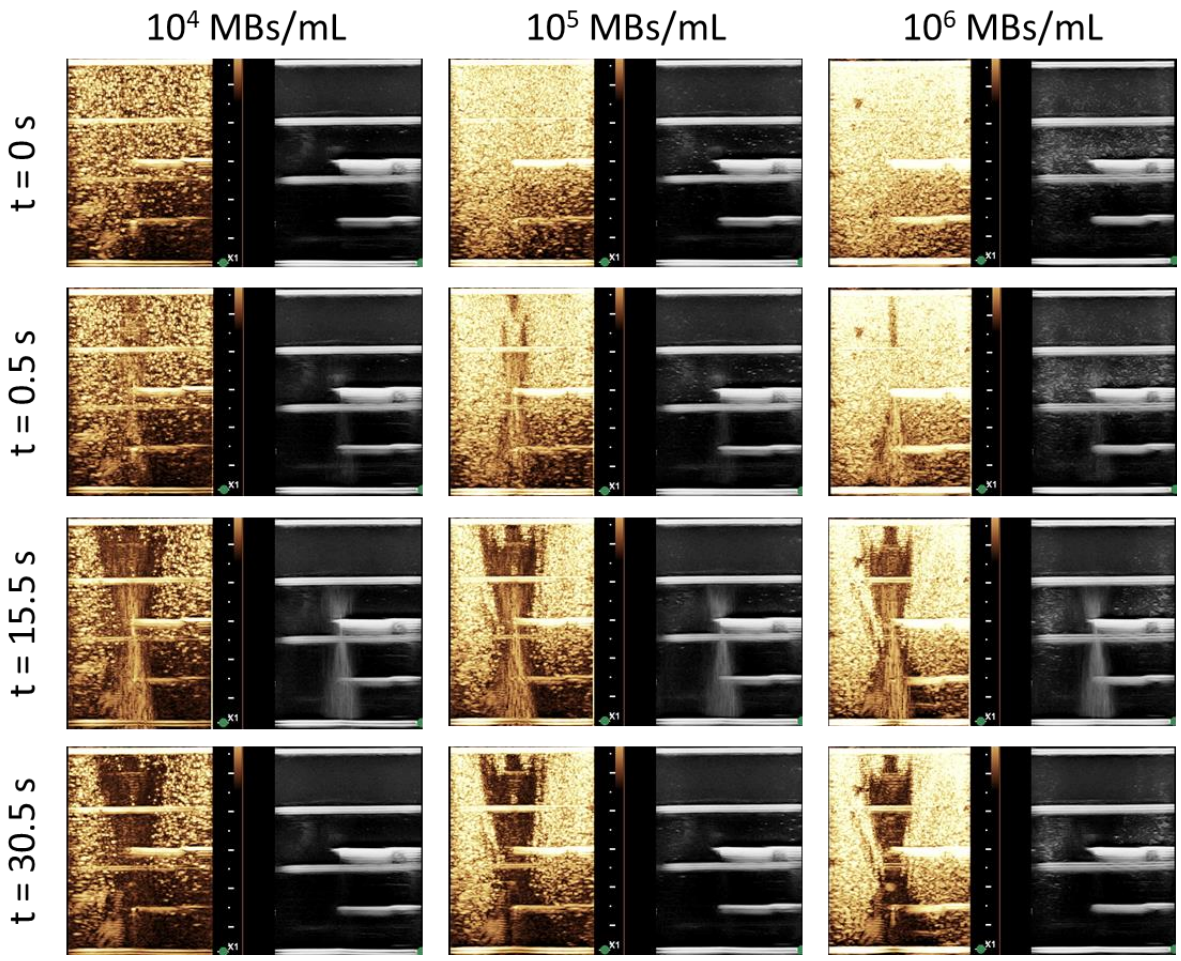

Figure 3.9. Ultrasound images acquired during heating with the focused transducer at 1.5 MPa focal pressure for three different microbubble concentrations. The left-side of each image are contrast ultrasound images whilst the right side are conventional fundamental B-mode images. The echoes in the contrast images are produced by the non-linear oscillation of microbubbles.

As shown in Figure 3.9, the RF artifact from our heating transducer is shown even when the transducer is no longer firing a heating pulse and the L12-3 is collecting an image (t = 0.5s, and t = 15.5 s). Figure 3.10 shows the ultrasound images taken from the three microbubble concentrations used in the heating experiments before any heating pulse has been fired (top row), after only a single heating pulse (400,000 cycle pulse, 1.074 MHz frequency, 2 MPa focal pressure instead of 1.5 MPa focal pressure) has been fired (middle row), and after 6 heating pulses that are fired every 500 ms (bottom row) to replicate the pulsing scheme used during heating experiments. After a single heating pulse (denoted as t = 0.5 s) was fired into the low concentration GEM phantom, it appeared that all of the microbubbles at the transducer's focus as well as some post-focally were eliminated; they cannot be seen in the contrast side of imaging. In the medium concentration, after a single heating pulse, most of the microbubbles at the transducer's focus were eliminated with some post focal destruction. At the highest concentration, after a single heating pulse, similar trends were observed in that the transducer was able to destroy a majority of the microbubbles pre focally and at the focus with minimal destruction past the focus. Comparing concentrations, the width of microbubble destruction at the focus decreased with increasing microbubble concentrations due to the phenomenon of acoustic shadowing. After firing 6 heating pulses, an hourglass outline can be seen, which means that most of the microbubbles in the beam path have been destroyed. Comparing a single heating pulse to after 6 heating pulses, the destruction at the focus, there was no noticeable difference in medium concentration. After 6 heating pulses in the high concentration, the destruction at the focus seemed to increase in width, suggesting that at the high concentration, there is enough microbubbles present at the focus to successfully attenuate the beam path preventing destruction of the microbubbles at the focus with a single heating pulse.

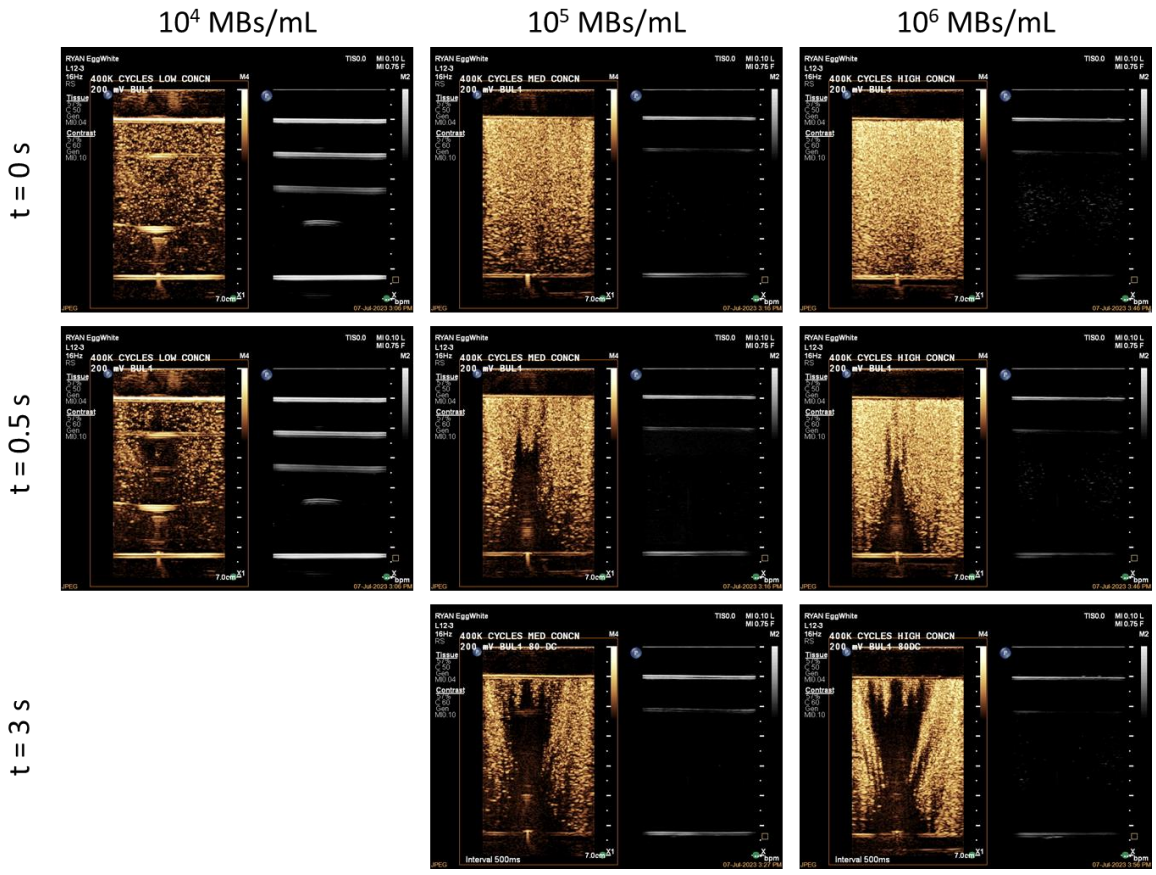

Figure 3.10. Ultrasound images acquired before firing any heating pulses (top row), after firing a single heating pulse (middle row), and after firing 6 heating pulses (10^4 MBs/mL was not used) with every pulse firing every 500 ms (bottom row) with our focused transducer at 2 MPa focal pressure for three different microbubble concentrations. The left-side of each image are contrast ultrasound images whilst the right side are conventional fundamental B-mode images.

Figure 3.11 shows ultrasound images taken from the three microbubble concentrations used in the heating experiments before any pulse has been fired and after a single pulse (1,000-100,000 cycle pulse, 1.074 MHz frequency, 2 MPa focal pressure) has been fired. At the low concentration (10^4 MBs/mL), after a single pulse is fired, most of the microbubbles at the focus are destroyed completely. As the number of cycles in the pulse fired is increased, post focal microbubble destruction occurs to a greater extent as well regardless of microbubble

concentration. During the first heating pulse (440,000 cycles), microbubble destruction occurs throughout the whole process. Thus, the microbubble concentration prefocally and at the focus changes continuously during the first heating pulse, which affects the attenuation via microbubbles, thus also affecting the experienced focal pressures. Henceforth, this suggests a transient relationship between microbubble concentration and focal pressure exists.

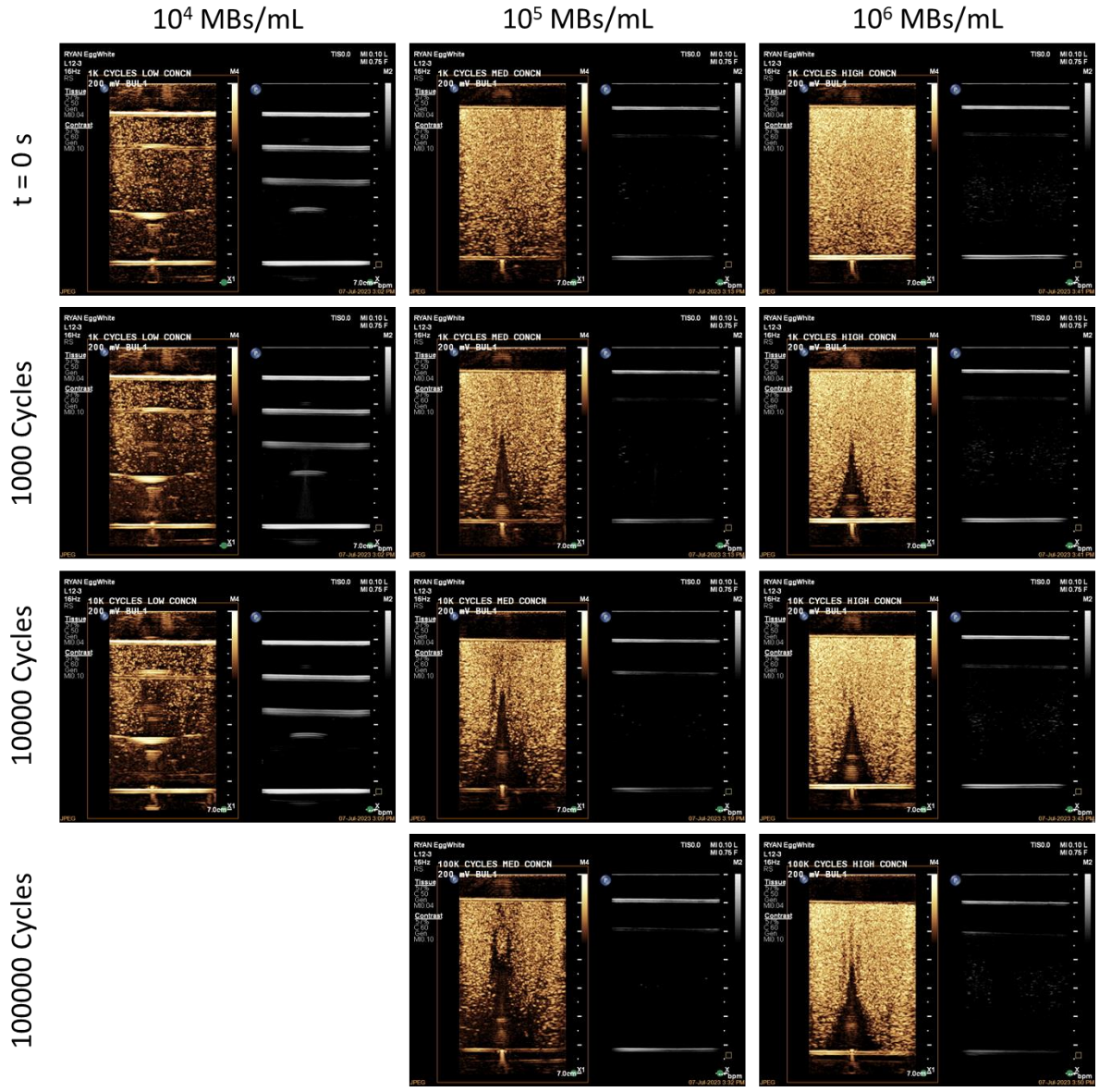

Figure 3.11 Ultrasound images acquired before firing any heating pulses (top row), after firing a single pulse of varying cycle length: 1,000 cycles, 10,000 cycles, and 100,000 cycles

at three different microbubble concentrations. The left-side of each image are contrast ultrasound images whilst the right side are conventional fundamental B-mode images.

Chapter 4. DISCUSSION

4.1 Difficulties with Thermocouple Measurements in Fluid Medium

In comparison to the solid gel media used in this work, fluid media were much easier to fabricate as the fluid medium in our work only involves mixing glycerol with water which was not as time consuming when compared to the gelatin-based phantoms, which required the mixing and heating of gelatin followed by the cooling and setting of the gelatin mixed fluid. In an ideal situation, the fluid used in our work would behave similar to a perfused organ. Thus, it would have similar acoustic properties to human tissue whilst allowing for dilution of microbubbles, free movement of microbubbles, and does not easily move when high amplitude pressure waves propagate through the fluid medium. In our work, the fluid's ability to not move easily when heated as well as the need for dilute microbubbles proved to be troublesome. The use of pure glycerol did not allow for successful dilution of microbubbles into the medium. This fluid medium did allow for successful administration of microbubble and was more prone to streaming, which makes aligning the thermocouple to the transducer's focus very difficult as we will still have a ± 0.5 mm error from our alignment technique and cannot reduce this error with low amplitude heating, which is easily possible with solid gel phantoms. The presence of streaming regardless of thermocouple misalignment can be seen in Figure 3.1. The measured heating curves greatly deviated in behavior with the modelled heating curves, which suggests that the fluid moves due to acoustic streaming since our model assumes that the heated medium is rigid in space. Despite these struggles, we still performed thermocouple measurements whilst

heating 66% glycerol-water mixture with varying concentrations of dilute microbubbles as shown in Figure 3.4 and 3.5. From our work, when heating at a focal pressure of 1 MPa, the highest microbubble concentration of 10^6 MBs/mL resulted in an elevated temperature rise of 2 ºC when comparing to the glycerol mixture without dilute microbubbles (Figure 3.4). In conclusion, despite the 66% glycerol-water mixture's susceptibility to acoustic streaming, thermocouple measurements can still show the effects that microbubble concentration has on bubble-enhanced heating.

4.2 Dependence of Bubble-enhanced Heating on Acoustic Pressure Amplitude and Microbubble Concentration

Prior work has investigated the effects of acoustic pressure amplitudes and microbubble concentration, however this work focused primarily on the aims of achieving ablative conditions and not achieving mild hyperthermia conditions. In addition, no group has performed heating measurements in a fluid medium diluted with microbubbles with the aim of achieving mild hyperthermia conditions. Our work investigated the effect of acoustic pressure amplitude and microbubble concentration with the aim of achieving mild hyperthermia conditions in both fluid and solid phantoms. In the 66% glycerol-water mixture, focal pressures of 1 and 1.5 MPa and a microbubble concentration range of 10^4-10^6 MBs/mL were investigated. Despite struggling with alignment and having a medium prone to acoustic streaming, we can draw some conclusions when looking at the initial seconds of heating. By doing this, we minimize the effects of acoustic streaming. When considering this, at the focal pressure of 1 MPa, 10^6 MBs/mL resulted in a highest temperature elevation within the first second of heating followed by 10^5 then 10^4 MBs/mL. Increasing the focal pressure to 1.5 MPa, a different trend is observed in which the lowest microbubble concentration of 10^4 MBs/mL resulted in the highest temperature elevation

within the first second of heating followed by 10^5 then 10^6 MBs/mL. At the lower focal pressure heating, the maximum measured temperature elevation is consistent with the early temperature rise trends. However, these trends do not follow through when looking at the higher focal pressure. Both 10^4 and 10^5 MBs/mL resulted in similar maximum measured temperature elevation whilst the highest concentration had the highest maximum measured temperature elevation. At 10^6 MBs/mL, our heating curve shows characteristics of convective heating. Prior studies have shown that heating with high acoustic pressure amplitudes and high microbubble concentrations resulted in acoustic shadowing. In this case, the transmitted sound is attenuated more quickly, resulting in heating prefocally. At our highest acoustic pressure and highest microbubble concentration, we suggest that acoustic shadowing has occurred, resulting in the pre focal fluid to heat the most, and the thermocouple at the focus is measuring temperature rise mainly from convection. Even though the measured temperature rise does not give us mild hyperthermia conditions, we successfully observed similar trends in fluids as in solids. Ideally, these experiments were repeated in a more attenuative fluid medium that can resist acoustic streaming more easily to give us a better understanding of how to achieve localized mild hyperthermia in a fluid medium.

As mentioned previously, thermocouple measurements in fluids that are easily susceptible to streaming were difficult. This resulted in our work to consider the usage of more solid gel phantoms. Acoustic property measurements of the gelatin-based phantoms used in this work showed that these media were much more representative of the acoustic properties experienced in humans in regard to speed of sound and density. The attenuation of the GEM phantom was closest to human tissue out of all the media used in this study and can easily be altered to become more similar to human tissue by increasing the percentage of evaporated milk used. Due to the

low acoustic attenuation of porcine gelatin phantoms, a higher acoustic pressure is needed for mild hyperthermia temperature rise (3 MPa). The presence of dilute microbubbles did enhance temperature rise and microbubble concentration did result enhancement in temperature elevation. To explore the role of acoustic pressure amplitude and microbubble concentration in a solid gel phantom, GEM phantoms were heated at focal pressures of 1 and 1.5 MPa with 3 varying microbubble concentrations. (Figure 3.7 and 3.8). When heating with a focal pressure of 1.5 MPa, the medium concentration had the highest enhancement in temperature rise followed by the low then high concentration, with the low and medium concentrations resulting in maximum measured temperature elevations that are sufficient for inducing mild hyperthermia. At the lower focal pressure of 1 MPa, no bubble-enhanced heating was measured. The high concentration resulted in the highest maximum temperature elevation when compared to the other microbubble concentrations; and is then followed by medium and low concentrations. Thus, at a focal pressure of 1 MPa, an ideal microbubble concentration may be higher than the high concentration used in our experiment for inducing enhanced temperature rises. Another possible explanation is that the *in situ* focal pressure has not reached a certain pressure threshold needed for inertial cavitation, such that bubble-enhanced heating at the focus occurs. The measurements also at the lower acoustic pressures varied greatly with the addition of microbubbles especially at the medium and high concentrations; thus, it may be useful to repeat these measurements. To summarize, regardless of medium being heated there exists a balance between acoustic pressure amplitude and microbubble concentrations in regard to enhancement of heating at the focus. A large enough acoustic pressure magnitude will be needed to inertially cavitate the microbubbles at the focus and the microbubble concentration has to be at an optimal concentration that does not cause heating to occur prefocally but still enough microbubbles to contribute to elevated

temperature rise. This optimal concentration changes with acoustic pressure amplitude, which can complicate the relationship between microbubble concentration and acoustic pressure amplitude for optimization of bubble-enhanced heating.

4.3 Importance of Imaging During High Intensity Focused Ultrasound Treatment

Unlike most other medical imaging modalities, ultrasound is able to provide images in real time. This allows for our heating treatment to be monitored in real time, giving us the ability to observe the path of microbubble destruction over time and the shape of our HIFU beam path, which can be seen in Figure 3.9 and Figure 3.10. In doing so, images of the microbubble destruction over time gives us insight into the transient role that microbubbles had in enhancing temperature elevation at the focus in solid and fluid media. From Figure 3.10, we observed that most of the microbubbles that are at the focus or proximal to the focus were destroyed after firing 6 heating pulses, which correlates to the immediate temperature elevation in media that contained microbubbles when compared to the media that did not contain microbubbles. Although our thermocouple alignment process does not require the use of imaging, the use of imaging will be pivotal as this work moves to *in vivo*. The ability to image the transducer's beam path via the RF artifact gives us a way to guide our transducer's focus to coincide with our treatment region. Even without the RF artifact, the real time monitoring of microbubble destruction allows us to understand where most of the heating has occurred and can adjust accordingly if needed. In conclusion, the use of ultrasound imaging will be important both as a tool for guiding before treatment and monitoring during treatment.

4.4 LIMITATIONS OF THIS WORK

The presented work has many limitations that have to be considered. First, being the media used in this work. By measuring the acoustic properties (speed of sound and density), we were able to determine that the 66% glycerol-water solution had acoustic properties highly different to human tissue whilst the porcine gelatin and GEM phantoms had speed of sound and densities similar to human tissue. Attenuation of these media were lower with GEM phantoms being the closest to human tissue; this value may be altered to better match with human tissue by increasing the percent composition of evaporated milk. However, the use of solid gel phantoms does depart from reality in that microbubbles are not trapped in space but are moving. Usage of a single thermocouple only allowed us to measure temperature at a single point in space and thus we are not able to quantify the enhancement in treatment volume (volume with temperature elevation above 5 ºC) due to the presence of diffuse microbubbles. We are able to suggest that there is an enhancement in treatment volume due to measured elevated heating at the focus and convection of that heat would increase the treatment volume. This could be alleviated by using volumetric temperature measurement techniques such as magnetic resonance temperature measurements or through the use of thermochromic dyes. Usage of magnetic resonance imaging is very costly and has reduced spatial and temporal resolution. Use of thermochromic dyes may also pose a challenge as the dye would be added around 30 ºC before the solution has fully set and placed in the refrigerator, which may prove to be a logistical challenge. Lastly, the major goal of this study was to investigate the effects of microbubble concentration and acoustic pressure amplitude in inducing localized temperature elevation relevant for mild hyperthermia. Since the microbubbles were diluted in our media, the lack of enhanced measured temperature elevation at the focus can be attributed to acoustic shadowing. There is a high enough microbubble concentration that

attenuates the beam path, such that the enhancement in heating occurs prefocally. Furthermore, as each successive pulse is fired or as the pulse length increases, microbubbles in the beam path are destroyed, which reduces the attenuation experienced by the sound beam, which will change the *in situ* focal pressure over time, further complicating our understanding of acoustic pressure amplitude and microbubble concentration. The issues caused by acoustic shadowing (more pronounced at high microbubble concentrations) may be alleviated by positioning our transducer's focus to be closer to the sides of the box instead of being at the center and taking thermocouple measurements there. This would reduce the distance that the beam path must travel within the GEM phantom, which would reduce the number of microbubbles that attenuate our beam prefocally. Thus, we have a model that better investigates microbubble concentration and acoustic pressure amplitude by minimizing the effects of acoustic shadowing, especially at high acoustic pressures and high microbubble concentrations. Nevertheless, we were able to measure the presence of bubble-enhanced heating in 3 media: 66% glycerol-water solution, porcine gelatin phantom, and GEM phantoms and was able to show conditions that resulted in the temperature rise relevant for mild hyperthermia in the GEM phantoms.

Chapter 5. CONCLUSION

Three tissue-mimicking fluid and solid gel media that allowed for uniform dilution of microbubbles were developed and characterized. Use of both fluid and solid gel media aided in studying bubble-enhanced heating as each type of medium had different benefits. The 66% glycerol-water solution was very easy to prepare and represented the case in which microbubbles could freely move in space, which tries to replicate circulating microbubbles, but was prone to acoustic streaming and had acoustic properties vastly different from human tissue. With the

gelatin-based solid gel phantoms, issues caused by acoustic streaming (bulk fluid movement) were eliminated. This phantom had acoustic properties similar to human tissue, however, the microbubbles were entrapped in space. Temperature elevation with and without dilute microbubbles of varying concentration and at different acoustic pressure amplitudes was measured. This was accomplished by developing a robust alignment technique that took advantage of pulse-echo from the heating transducer and the thermocouple and transducer geometry, resulting in very accurate thermocouple alignment with ± 0.5 mm misalignment error when adjusting via low-amplitude heating. In doing so, we were able to identify optimal parameters that resulted in mild hyperthermia (5-10 ºC temperature elevation). Temperature elevation relevant for mild hyperthermia was only measured in the GEM phantoms, as the other media had low attenuation and/or acoustic streaming but still showed presence of bubble-enhanced heating. In the GEM phantom, we measured bubble-enhanced heating that resulted in mild hyperthermia temperature requirements at the focus (5.65 and 6.11 ºC) when heating at a focal pressure of 1.5 MPa at the low and medium microbubble concentrations respectively, but not at the high concentration. This was not observed when heating at a lower focal pressure regardless of microbubble concentrations. Through imaging, we were able to observe in real-time the path of microbubble destruction through each consecutive heating pulse. Most of the microbubbles at the focus are destroyed during the first three seconds (~6 heating pulses), which was shown in the enhanced temperature elevation of media that had microbubbles when compared to those that did not. We observed that the microbubble destruction path changes as microbubble concentration changes, which affects how much heating happens as well as where heating occurs in the media. During our first heating pulse, continual microbubble destruction throughout the pulse changes the concentration of microbubbles before the focus as well as at the

focus, which affects the experienced focal pressure. In conclusion, bubble-enhanced heating was measured in 3 media: 1 fluid and 2 solid gel phantoms, which demonstrated the importance of microbubble concentration and acoustic pressure amplitude for optimal enhancement in localized heating for inducing mild hyperthermia temperatures.

BIBLIOGRAPHY

[1] G. Cooper, "The Development and Causes of Cancer - The Cell - NCBI Bookshelf," *U.S National Library of Medicine*, 1970. https://www.ncbi.nlm.nih.gov/books/NBK9963/ (accessed Jun. 04, 2022).

[2] H. Sung *et al.*, "Global cancer statistics 2020: GLOBOCAN estimates of incidence and mortality worldwide for 36 cancers in 185 countries," *CA Cancer J Clin*, 2021, doi: 10.3322/caac.21660.

[3] R. L. Siegel, K. D. Miller, N. S. Wagle, and A. Jemal, "Cancer statistics, 2023," *CA Cancer J Clin*, vol. 73, no. 1, pp. 17–48, Jan. 2023, doi: 10.3322/CAAC.21763.

[4] M. Arruebo *et al.*, "Assessment of the Evolution of Cancer Treatment Therapies," *Cancers (Basel)*, vol. 3, no. 3, p. 3279, Sep. 2011, doi: 10.3390/CANCERS3033279.

[5] C. Pucci, C. Martinelli, and G. Ciofani, "Innovative approaches for cancer treatment: current perspectives and new challenges," *Ecancermedicalscience*, vol. 13, Sep. 2019, doi: 10.3332/ECANCER.2019.961.

[6] B. Mansoori, A. Mohammadi, S. Davudian, S. Shirjang, and B. Baradaran, "The Different Mechanisms of Cancer Drug Resistance: A Brief Review," *Adv Pharm Bull*, vol. 7, no. 3, p. 339, 2017, doi: 10.15171/APB.2017.041.

[7] N. Nomikou, Y. S. Li, and A. P. McHale, "Ultrasound-enhanced drug dispersion through solid tumours and its possible role in aiding ultrasound-targeted cancer chemotherapy," *Cancer Lett*, vol. 288, no. 1, pp. 94–98, Feb. 2010, doi: 10.1016/J.CANLET.2009.06.028.

[8] E. Henke, R. Nandigama, and S. Ergün, "Extracellular Matrix in the Tumor Microenvironment and Its Impact on Cancer Therapy," *Front Mol Biosci*, vol. 6, p. 470149, Jan. 2020, doi: 10.3389/FMOLB.2019.00160/BIBTEX.

[9] M. Schober *et al.*, "Desmoplasia and Chemoresistance in Pancreatic Cancer," *Cancers 2014, Vol. 6, Pages 2137-2154*, vol. 6, no. 4, pp. 2137–2154, Oct. 2014, doi: 10.3390/CANCERS6042137.

[10] J. A. Conti *et al.*, "The Desmoplastic Reaction Surrounding Hepatic Colorectal Adenocarcinoma Metastases Aids Tumor Growth and Survival via αv Integrin Ligation," *Clinical Cancer Research*, vol. 14, no. 20, pp. 6405–6413, Oct. 2008, doi: 10.1158/1078-0432.CCR-08-0816.

[11] C. W. Schultz *et al.*, "Selecting the optimal parameters for sonoporation of pancreatic cancer in a pre-clinical model," *Cancer Biol Ther*, vol. 22, no. 3, pp. 204–215, 2021, doi: 10.1080/15384047.2021.1881026/SUPPL_FILE/KCBT_A_1881026_SM9789.ZIP.

[12] D. Bressand *et al.*, "Enhancing Nab-Paclitaxel Delivery Using Microbubble-Assisted Ultrasound in a Pancreatic Cancer Model," *Mol Pharm*, vol. 16, no. 9, pp. 3814–3822, Sep. 2019, doi: 10.1021/ACS.MOLPHARMACEUT.9B00416/ASSET/IMAGES/LARGE/MP9B00416_0005.JPEG.

[13] S. Snipstad *et al.*, "Sonopermeation Enhances Uptake and Therapeutic Effect of Free and Encapsulated Cabazitaxel," *Ultrasound Med Biol*, vol. 47, no. 5, pp. 1319–1333, May 2021, doi: 10.1016/J.ULTRASMEDBIO.2020.12.026.

[14] C. Y. Lin, J. R. Li, H. C. Tseng, M. F. Wu, and W. L. Lin, "Enhancement of focused ultrasound with microbubbles on the treatments of anticancer nanodrug in mouse tumors," *Nanomedicine*, vol. 8, no. 6, pp. 900–907, Aug. 2012, doi: 10.1016/J.NANO.2011.10.005.

[15] S. Kotopoulis *et al.*, “Sonoporation-enhanced chemotherapy significantly reduces primary tumour burden in an orthotopic pancreatic cancer xenograft,” *Mol Imaging Biol*, vol. 16, no. 1, pp. 53–62, Feb. 2014, doi: 10.1007/S11307-013-0672-5/METRICS.

[16] S. Eggen, M. Afadzi, E. A. Nilssen, S. B. Haugstad, B. Angelsen, and C. de L. Davies, “Ultrasound Improves the Uptake and Distribution of Liposomal Doxorubicin in Prostate Cancer Xenografts,” *Ultrasound Med Biol*, vol. 39, no. 7, pp. 1255–1266, Jul. 2013, doi: 10.1016/J.ULTRASMEDBIO.2013.02.010.

[17] S. Snipstad *et al.*, “Ultrasound Improves the Delivery and Therapeutic Effect of Nanoparticle-Stabilized Microbubbles in Breast Cancer Xenografts,” *Ultrasound Med Biol*, vol. 43, no. 11, pp. 2651–2669, Nov. 2017, doi: 10.1016/J.ULTRASMEDBIO.2017.06.029.

[18] Y. Wang *et al.*, “Clinical study of ultrasound and microbubbles for enhancing chemotherapeutic sensitivity of malignant tumors in digestive system,” *Chinese Journal of Cancer Research*, vol. 30, no. 5, pp. 553–563, 2018, doi: 10.21147/J.ISSN.1000-9604.2018.05.09.

[19] G. Dimcevski *et al.*, “A human clinical trial using ultrasound and microbubbles to enhance gemcitabine treatment of inoperable pancreatic cancer,” *Journal of Controlled Release*, vol. 243, pp. 172–181, Dec. 2016, doi: 10.1016/J.JCONREL.2016.10.007.

[20] S. R. Sirsi and M. A. Borden, “Microbubble Compositions, Properties and Biomedical Applications,” *Bubble Sci Eng Technol*, vol. 1, no. 1–2, p. 3, 2009, doi: 10.1179/175889709X446507.

[21] R. D. Issels *et al.*, “Neo-adjuvant chemotherapy alone or with regional hyperthermia for localised high-risk soft-tissue sarcoma: a randomised phase 3 multicentre study,” *Lancet Oncol*, vol. 11, no. 6, p. 561, Jun. 2010, doi: 10.1016/S1470-2045(10)70071-1.

[22] P. Wust *et al.*, “Hyperthermia in combined treatment of cancer,” *Lancet Oncology*, vol. 3, no. 8, pp. 487–497, 2002, doi: 10.1016/S1470-2045(02)00818-5.

[23] M. Dunne, M. Regenold, and C. Allen, “Hyperthermia can alter tumor physiology and improve chemo-and radio-therapy efficacy,” 2020, doi: 10.1016/j.addr.2020.07.007.

[24] Y.-F. Zhou, “High intensity focused ultrasound in clinical tumor ablation,” *World J Clin Oncol*, vol. 2, no. 1, p. 8, Jan. 2011, doi: 10.5306/WJCO.V2.I1.8.

[25] M. Rohani and A. Fasano, “Focused Ultrasound for Essential Tremor: Review of the Evidence and Discussion of Current Hurdles,” *Tremor and Other Hyperkinetic Movements*, vol. 7, 2017, doi: 10.7916/D8Z89JN1.

[26] Z. Izadifar, Z. Izadifar, D. Chapman, and P. Babyn, “An Introduction to High Intensity Focused Ultrasound: Systematic Review on Principles, Devices, and Clinical Applications,” *J Clin Med*, vol. 9, no. 2, 2020, doi: 10.3390/jcm9020460.

[27] A. Clark, S. Bonilla, D. Suo, Y. Shapira, and M. Averkiou, “Microbubble-Enhanced Heating: Exploring the Effect of Microbubble Concentration and Pressure Amplitude on High-Intensity Focused Ultrasound Treatments,” *Ultrasound Med Biol*, vol. 47, no. 8, pp. 2296–2309, Aug. 2021, doi: 10.1016/J.ULTRASMEDBIO.2021.03.035.

[28] E. K. Juang, L. H. De Koninck, K. S. Vuong, A. Gnanaskandan, C.-T. Hsiao, and M. A. Averkiou, “Controlled Hyperthermia With High-Intensity Focused Ultrasound and Ultrasound Contrast Agent Microbubbles in Porcine Liver,” *Ultrasound Med Biol*, vol. 49, pp. 1852–1860, 2023, doi: 10.1016/j.ultrasmedbio.2023.04.015.

[29] H. H. Pennes, “Analysis of tissue and arterial blood temperatures in the resting human forearm,” *J Appl Physiol*, vol. 85, no. 1, 1998, doi: 10.1152/jappl.1998.85.1.5.

[30] A. I. Farrer *et al.*, “Characterization and evaluation of tissue-mimicking gelatin phantoms for use with MRgFUS,” *J Ther Ultrasound*, vol. 3, no. 1, pp. 1–11, Jun. 2015, doi: 10.1186/S40349-015-0030-Y/TABLES/4.

[31] I. De Cock *et al.*, “Ultrasound and microbubble mediated drug delivery: Acoustic pressure as determinant for uptake via membrane pores or endocytosis,” 2014, doi: 10.1016/j.jconrel.2014.10.031.

[32] M. L. De Temmerman *et al.*, “mRNA-Lipoplex loaded microbubble contrast agents for ultrasound-assisted transfection of dendritic cells,” *Biomaterials*, vol. 32, no. 34, pp. 9128–9135, Dec. 2011, doi: 10.1016/J.BIOMATERIALS.2011.08.024.

[33] S. Kotopoulis *et al.*, “SonoVue® vs. Sonazoid™ vs. Optison™: Which Bubble Is Best for Low-Intensity Sonoporation of Pancreatic Ductal Adenocarcinoma?,” *Pharmaceutics*, vol. 14, no. 1, Jan. 2022, doi: 10.3390/PHARMACEUTICS14010098/S1.

[34] M. A. Averkiou, M. F. Bruce, J. E. Powers, P. S. Sheeran, and P. N. Burns, “Imaging Methods for Ultrasound Contrast Agents,” *Ultrasound Med Biol*, vol. 46, no. 3, pp. 498–517, Mar. 2020, doi: 10.1016/J.ULTRASMEDBIO.2019.11.004.

[35] F. A. Duck, “Acoustic Properties of Tissue at Ultrasonic Frequencies,” *Physical Properties of Tissues*, pp. 73–135, 1990, doi: 10.1016/B978-0-12-222800-1.50008-5.

[36] J. Fujino and T. Honda, “Measurement of Specific Heat Capacity of Gelatin for Human Phantom using Differential Scanning Calorimetry”.

[37] T. Sakiyama, S. Han, A. Torii, O. Miyawaki, and T. Yano, “Intrinsic Thermal Conductivity of Gelatin Estimated Independently of Heat Conduction Models,” *http://dx.doi.org/10.1080/00021369.1991.10870602*, vol. 55, no. 2, pp. 487–492, 2014, doi: 10.1080/00021369.1991.10870602.

[38] Y. B. Pottathara *et al.*, “Solidification of Gelatine Hydrogels by Using a Cryoplatform and Its Validation through CFD Approaches,” *Gels*, vol. 8, no. 6, Jun. 2022, doi: 10.3390/GELS8060368.